# Cavitation Induction by Projectile Impacting on a Water Jet

E. Stavropoulos Vasilakis[a,*], N. Kyriazis[a], P. Koukouvinis[a], M.Farhat[b], M. Gavaises[a]

[a] *School of Mathematics, Computer Science and Engineering, CITY, University of London, UK*
[b] *Laboratory of Hydraulic Machines, EPFL, CH*

**Abstract**

The present paper focuses on the simulation of the high-velocity impact of a projectile impacting on a water-jet, causing the onset, development and collapse of cavitation. The simulation of the fluid motion is carried out using an explicit, compressible, density-based solver developed by the authors using the OpenFOAM library. It employs a barotropic two-phase flow model that simulates the phase-change due to cavitation and considers the co-existence of non-condensable and immiscible air. The projectile is considered to be rigid while its motion through the computational domain is modelled through a direct-forcing Immersed Boundary Method. Model validation is performed against the experiments of Field et al. [1], who visualised cavity formation and shock propagation in liquid impacts at high velocities. Simulations unveil the shock structures and capture the high-speed jetting forming at the impact location, in addition to the subsequent cavitation induction and vapour formation due to refraction waves. Moreover, model predictions provide quantitative information and a better insight on the flow physics that has not been identified from the reported experimental data, such as shock-wave propagation, vapour formation quantity and induced pressures. Furthermore, evidence of the Richtmyer-Meshkov instability developing on the liquid-air interface are predicted when sufficient dense grid resolution is utilised.

*Keywords:* Cavitation, Shock Waves, liquid-solid impacts, liquid-gas interface, Richtmyer-Meshkov instability

## 1. Introduction

Liquid impacts on solids involve physical problems of high engineering interest, as they are linked with erosion development [1] and eventual damage of

*Corresponding author
*Email address:* evangelos.stavropoulos-vasilakis@city.ac.uk (E. Stavropoulos Vasilakis)

mechanical structures and machines; therefore, they are of interest to a wide range of hydraulic machinery utilised in many industrial applications. Cavitation formation and induced erosion can be also realised during the impact of liquid droplets on steam-turbine blades [2], and rain droplets impacting on airplanes [3] and wind-turbine blades [4]. Moreover, shock-wave interaction with material interfaces has been extensively demonstrated in e.g. underwater explosions [5] and spark/laser-generated bubbles [6], or the excitation of pre-existing nuclei by acoustic pulses [7]. The interaction of shocks with liquid-gas interfaces has been thoroughly investigated and complex wave structures have been identified by numerous researchers [8, 9, 10, 11, 12, 13]. Many experimental works on the mechanisms and the dynamics of liquid-to-liquids impacts [14, 15] or liquid-to-solid impacts [16], where solid compliance [17], deformation [18, 19, 20] or fracture [21] are also investigated, have established a solid understanding of the phenomena taking place, pinpointing cavitation formation due to pressure waves as one of the main causes of erosion.

Such interactions between waves and interfaces have also applications in the medical and bioengineering fields [10]. For example, High Intensity Focused Ultrasound (HIFU) [22, 23, 24] is a non-invasive technique which relies on the production of strong pressure waves that induce the formation and collapse of cavities within tissues. The strong forced oscillations of such cavities lead to extreme localized heating and malignant tissue destruction (histotripsy) or the destruction of solid material, termed as stone (lithotripsy). Interactions of shock waves with soft matter and bubbles occur also in brain injuries caused during mild domestic explosions [24, 25] and common head concussion accidents [26, 27] happening in everyday life. There are even animal species that have evolved to exploit the generation of shock waves through cavitation to stun or kill prey (snapping and mantis shrimps [28, 29]).

The interaction of shock-waves with liquid-gas interfaces in fast-slow configurations (i.e. shock initially travelling in a liquid), has been also established through computational studies, which have been validated against experiments such as those reported in [8, 9]. These studies demonstrate that compression waves are always reflected as expansion waves upon hitting the interface [9], which may lead to cavitation formation. The link between the reflected wave type and the acoustic impendence ration is clearly demonstrated in [30], in the form of two asymptotic scenarios. According to this study, the first scenario involves a wave travelling in a material and interacting with a perfectly rigid wall (infinite acoustic impedance); in that case the wave is reflected back at the same amplitude. The second case involves interaction of the wave with perfect vacuum (acoustic impedance of zero); in that case the wave is reflected back with opposite amplitude. A comprehensive summary of the experimental findings on liquid to liquid or solid impacts can been found in [1]; the study, highlights the complicated wave structures interacting with free-surfaces and the potential of cavitation erosion development.

Along the same lines, the theoretical study of [31], has analytically examined the liquid drop impacts on solid surfaces, while the experiments reported in [1] for liquid droplets impacting on a solid surface, reveal the strong effects of com-

pressibility that take place locally in the liquid bulk near the impact region. A peak in pressure can be observed and a complicated shock wave structure is developing, while high-speed jetting may occur at the impact location; at the same time, rarefaction waves form that may create enough tensile stress to induce cavitation within the liquid. The high-speed jetting characteristics have been investigated experimentally by Thoroddsen et al. [32] using free-falling spheres that impact on a liquid pool; the authors tried to link the Reynolds number with the jets' velocity and the shape of the lamella formed during splashing. Fractures of solid surfaces by liquid or solid impacts and shock-waves have been studied by Bowden et al [21].

On the modelling side, droplet impact on solid surfaces has been investigated numerically by many researchers using various numerical algorithms to account for the different phases, such as marker-and-cell (MAC) finite differences [33], front tracking approach [12], Volume of Fluid [34], multicomponent Euler solver [35] or two-fluid model for Euler equations [36], to name a few. Sanada et al. [35] investigated the impact of a liquid droplet on solid surface, the shock-wave structures, interfaces and jetting as well as solid surface compliance. Harvie et al [34] modelled the drop impact on hot solid surfaces, focusing both on dynamics of the impact as well as the heat transfer. A detailed numerical work on shock-wave formation upon the impact of a droplet on rigid wall has been presented by Haller et al. [12], where they unveil the complex shock structure of the multiple overlapping waves that interact with the free surface and the moving contact line between the wall and the droplet. Moreover, the investigation of [13] has focused on the shock confinement inside isolated liquid volumes and proposed a new model for erosion based on cavitation caused by trapped shocks. However, cavitation is not modelled in the aforementioned works, although the work of [36] identifies the potential vapour regions. Cavitation induction during droplet impact on wall is studied by [37], where numerical results are compared to experimental findings from literature and found in good agreement.

Despite the importance of the underlying physical phenomena, it is clear from the above literature that limited information exists on quantifying the phenomena following liquid-to-solid impact that lead to cavitation, while there are no studies so far that simulate the combined motion of impinging solid objects onto liquids together with the induced cavitation. The present study aims to fill this gap in the existing literature. More specifically, it focuses on the simulation of a high-velocity impact of a solid projectile on a water-jet and investigates the shock-wave formation, structures and the cavitation induction; as already mentioned,this case has been recently studied experimentally [1] by one of the co-authors of this paper and his co-workers; relevant simulations are presented in the present work for the first time supported by further experimental data, which are utilised here for validation of the developed numerical framework. The experiment under consideration refers to an impact where the water target is wider than the solid surface. This comes to a contrast with the usual liquid-to-solid impact configuration, which is comprised by a small water droplet and a very wide solid wall, studied by numerous researchers, including [1, 16, 35, 38]. This difference in blockage of the flow is expected to affect the

physics of the impact, as the water target being wider than the projectile, lets more room to the liquid to expand. Impacts with low-blockage ratio, where a solid sphere drops into a liquid pool, are studied experimentally by Thoroddsen et al. [32], who focused on the relationship of the impact jetting with Reynolds number and observed differences with high-blockage cases of drop impacts on wall [16, 31]. They studied impacts at lower velocities and did not investigated cavitation initiation or shock structures. The current study tries to shed light in low-blockage impact phenomena at high velocities and assess similarities to the high-blockage impacts regarding shock, vapour and jetting structures. Moreover, the simulation of this impact case poses a significant challenge regarding the coupled problem of solid projectile motion and the induced complex flow field that has interfaces and is subject to phase-change. To tackle this issue, an Immersed Boundary (IB) Method is used to model the presence of a solid boundary onto the fixed grid of the domain, avoiding any complexities arising from re-meshing or moving-mesh techniques.

IB methods were introduced to model internal boundaries by either changing the computational stencil near the solid or adding source terms in the equations [39, 40]. The Immersed Boundary (IB) method used in this study, falls in the category of direct-forcing methods [40], where the presence of the boundary is taken into account as solid forcing by introducing a source term in the momentum equation. A similar method developed has been used in high velocity compressible turbulent flows by Mochel et al. [41], as well as by the authors to simulate the cavitating flow resulting from the high-speed closure of the claw of the pistol shrimp [28]. To the best of the authors' knowledge, apart from the method presented in [28], other studies employing an IB method for cavitating flows, such as Diesel injector flows with closing needle [42], or underwater motion of a projectile [43, 44], follow a cut cell methodology. The IB method used in the present study provides important advantages regarding geometrical and topological manipulations, compared to cut-cell methods. Forcing source terms are added in the momentum equations of an explicit density-based in-house compressible multiphase solver [37]. The solver is developed using the OpenFOAM platform [45], which provides a complete Computational Fluid Dynamics (CFD) framework, with its own programming pseudo-language that facilitates equation declaration, discretization and solution, and a rich library of models and functionalities, which ease the researcher to combine different components and develop novel numerical tools. The developed flow solver accounts for a gaseous phase and a liquid-vapour mixture, where the gas is considered as non-condensable and immiscible media, whereas phase-change is considered between the liquid and vapour phases by utilising a barotropic model. The developed solver follows a density-based approach, since cavitating flows have a large variation over the speed of sound, with a Mach number ranging from 1 up to 100 (in the liquid/vapour mixture region) [46, 47]. Whereas more common pressure-based solvers can handle such flows, the large variability in the speed of sound in the transition from liquid to liquid/vapour mixture make convergence difficult, since the speed of sound is used for the density correction corresponding to the pressure correction. Thus, the proposed density-based methodology offers ro-

bustness and fast, explicit time marching. Moreover, a hybrid numerical flux is proposed that makes the solver suitable for a wide range of Mach numbers, even low-Mach flows where usually the density-based yield issues. It is highlighted that such solvers are not available in the open literature, since multiphase flows are commonly treated with pressure-based methodologies. The solver is aimed to be used on problems where surface tension does not play an important role compared to inertial or compressibility phenomena, such as high-speed solid-to-liquid impacts studied here. Therefore, surface tension is neglected.

A three-dimensional computational study is performed and numerical data are extracted that are qualitatively compared to the experimental observations, but also provide a more detailed insight on the vapour generation, growth and collapse upon the impact, as well as, a series of two-dimensional simulations is performed to investigate the shock and rarefaction waves structures, along with the high-speed jetting, in more detail.

The following section of the paper explains the developed numerical methodology, followed by presentation of the obtained results; the most important conclusions are summarised at the end.

## 2. Methodology

### *2.1. IB methodology*

The immersed solid boundary utilised here is represented by a surface mesh while a colour function is used to indicate the solid cells or *IB cells*, the computational grid cells are enclosed by this surface. As the tool is developed within the OpenFOAM library, an octree-search algorithm is used to initially find the grid cells with the cell centre lying inside the IB shell; then the solid stencil is extended to include the grid cells cut by the IB surface. The colour function *(IB mask)* representing the solid area, corresponds to the solid volume fraction of the cells and is calculated as the ratio of the cell volume covered by the IB surface over the total cell volume. This function receives values between 0 for fluid cells and 1 for solid cells. This calculation is carried out as the average of normal distance between all the vertices of the cell and the nearest IB surface face [28].

The forcing source term is calculated as the difference of the fluid velocity from the IB solid velocity, and therefore tends to impose no-slip condition on the IB cells. The source term is then multiplied with the IB mask to localise the IB forcing, as in equation 2.1.

$$\vec{f}_{IB} = \alpha_{IB} \cdot \rho \cdot \frac{U_{fluid} - U_{IB}}{\Delta t} \ , \quad \alpha_{IB} \in [0, 1] \tag{2.1}$$

The proposed forcing method, exhibits some advantages over the cut-cell methodologies used by other researchers [42, 43, 44]. The later methodologies cut the grid cells at the intersection with the solid surface by splitting the existing cell faces and creating a new face from triangulation of the intersection edges. This alters the topology of the cells as from hexahedral can become

tetrahedral or polyhedral and may produce very small cells. The geometrical manipulations ask for high-precision operations and the change in topology may affect the computations, as well as any small cells may introduce noise and spurious oscillations, although counter-actions have been proposed [48]. The proposed approach, assists the stability of the solver by adding a localised volumetric source term constant along the entire cell in the discretised equations, smoothens the source term introduction to the new cells if the solid is moving by using a continuous mask from 0 (*fluid cell*) to 1 (*IB cell*), and simplifies the geometrical computations by disregarding the precise solid surface and the grid intersection.

### *2.2. IB model coupling with flow*

The IB forcing term is introduced in the compressible Euler equations 2.2 that are solved using a density based, two-phase, explicit solver [37], that considers phase-change at constant temperature. The solver models a mixture of immiscible gas with a liquid-vapour mixture, using the Homogeneous Mixture approach, so that all phases are in mechanical and thermodynamic equilibrium. It takes into account phase change between the liquid and vapour phases according to a thermodynamic model. Temperature effects are neglected. This is because for the for the simulation presented here, according to thermodynamic tables for water, temperature variation can be expected less than $10^oC$ and only locally for a short time instant. More specifically, the minimum and maximum pressures calculated are $1350Pa$ and $2.4 \cdot 10^8 Pa$, respectively; these would translate in $\Delta T_{low} = 10K$ cooling and $\Delta T_{high} = 5K$ heating, tacking as $P_{ref} = 10^5 Pa$ and $T_{ref} = 293K$ as reference, respectively.

The mixture density ($\rho$) is calculated by equation 2.3, as function of the volume fractions of liquid mixture $\beta_{lm}$ , vapour $\alpha_v$ and gas $\beta_g$ , and the density of each phase ($\rho_l$ for the liquid, $\rho_v$ for the vapour, $\rho_g$ for the gas). Phase change between liquid and vapour is considered, using the linear barotropic law to compute the mixture density, as function of the saturation pressure ($p_{sat}$) and density ($\rho_{l,sat}$) of the liquid and the speed of sound ($c_l$ for the liquid and $c_v$ for the vapour) from equation 2.4. The gas is assumed to undergo an isothermal process; its density is computed by the ideal gas equation of state 2.5, for a given pressure ($p$) at a given temperature ($T_{ref}$), using the gas constant ($R_g$).

Moreover, the transport equation 2.6 is solved for the gas mass fraction $Y_g$ , in order to advect the gaseous phase. Surface tension does not play a significant role in the case studied here, because for the high velocity impact of the projectile on the water-jet, the Weber number is high, $We = \rho_{air} U^2_{impact} D_{jet}/\sigma = 1.85 \cdot 10^5$ ,considering $\sigma = 7.2 \cdot 10^{-2} Nm$ the surface tension between water and air. Therefore, the solver does not use any interface reconstruction or sharpening technique and the interface between liquid mixture and gas is slightly diffused and occupies a few cells (between 2 and 4). A similar approach for the advection of gas phase is used to simulate the cavitating flow through a nozzle and the primary breakup of the liquid jet in [49, 50].

The solver is making use of a special hybrid flux calculation, to tackle issues arising when density-based solvers are used for three-phase cases with great

variations of speed of sound. The hybrid flux is based on Primitive Variable Riemann Solver and Mach consistent flux [37, 51]. The reader is referred to [37] where the solver is presented in detail.

As the projectile velocity is relatively high resulting in a high Reynolds number of $Re = D_{jet}U_{impact}/\nu_{air} = 1.2 \cdot 10^5$, the inertial phenomena are dominant, the boundary layers are expected to be very thin and the turbulent scales very small to be captured but also to affect the dynamics of the impact. Turbulence is therefore not modelled and the viscosity is neglected.

$$\frac{\partial \vec{U}}{\partial t} + \frac{\partial F_k(\vec{U})}{\partial x_k} = \vec{S},\ in\ \Omega_f, \quad k = x, y, z \tag{2.2}$$

where

$\vec{U}$ is the vector of conservative variables $[\rho\ \rho Y_g\ \rho u_x\ \rho u_y\ \rho u_z]^T$

$\bar{\bar{F}}_k,\ k = x, y, z$ is the flux tensor

$\vec{S}$ is the vector of sources $[0\ 0\ f_{IBx}\ f_{IBy}\ f_{IBz}]^T$

$\Omega_f$ is the fluid domain

$$\rho = \beta_{lm} \cdot \Big((1 - \alpha_v)\rho_l + \alpha_v \rho_v\Big) + \beta_g \cdot \rho_g \tag{2.3}$$

$$\rho_{lm} = \rho_{l,sat} + \frac{p - p_{sat}}{c^2}, \quad c = \begin{cases} c_l, & p \geq p_{sat} \\ c_v, & p < p_{sat} \end{cases} \tag{2.4}$$

$$\rho_g = \frac{p}{R_g \cdot T_{ref}} \tag{2.5}$$

$$\frac{\partial \rho Y_g}{\partial t} + \nabla \cdot (\vec{U}\rho Y_g) = 0 \tag{2.6}$$

## 3. Test case description

### *3.1. 3-D configuration*

Both 3-D and 2-D cases have been simulated. The 3-D test case simulated can be seen in Figure 1. A projectile, with a diameter of $9mm$ is traveling at a speed of 210m/s towards the still water-jet target of $25mm$ diameter; the water falls vertically down under the influence of gravity, at a velocity of approximately 1m/s. The computational domain is chosen to be a cylinder with $4 \times D_{jet}$ diameter and $3.6 \times D_{jet}$ height, where $D_{jet}$ the diameter of the water-jet (fig. 1a). The domain is discretized with 128 equally spaced cells along the jet diameter (fig. 1b). The same cell width is maintained in the vicinity of the water-jet and then a cell expansion ratio of 1.2 is applied towards the cylindrical far-field. This discretization results in 2.9 million cells and ensures approximately equal sized cells in the water region, where all the phenomena of interest occur.

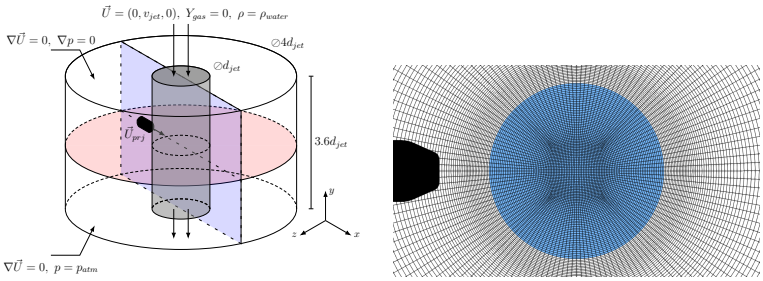


**Figure 1:** The three-dimensional computational domain (a) and the cylindrical mesh on the horizontal section (b), used in the three-dimensional simulation of projectile impact on vertical water-jet. Constant atmospheric pressure boundary condition is assigned on the periphery of the cylindrical domain and Neumann boundary conditions for both pressure and velocity are imposed on the top and bottom patches. Constant velocity, gas mass fraction and density values are placed on the water-jet inlet. The horizontal (red) and vertical (blue) mid-planes, where the results are presented on the following sections, are also shown.

The flowing water-jet is placed in the middle of the domain. The projectile commences to move instantaneously and impacts the jet after approximately $34\mu s$. A non-dimensional time scale is introduced, using the diameter of the jet $D_{jet} = 25mm$ and the speed of sound in the liquid $C_{water} = 1482.35^{m}/_{s}$, with respect to the time of impact: $\bar{\tau} = (t - t_{impact}) \cdot C_{water}/D_{jet}$.

The ambient air is initially stationary. The pressure of the domain is considered equal to $1bar$ and the reference temperature set to $300K$. The Mach number with respect to the surrounding air is 0.6 and with respect to the impacted water 0.14.

### *3.2. 2-D configurations*

Since the resolution required for a full 3-D simulation limits the model predictions to scales that do not allow high resolution of the liquid-gas interface in affordable CPU times, two-dimensional simulations have been also performed. In these cases, the projectile is impacting a static water planar section of the jet. This set-up corresponds to the horizontal symmetry plane of the projectile of the three-dimensional set-up. A rectangular area $6.4D_{jet} \times 3.6D_{jet}$ is chosen as the computational domain, where $D_{jet}$ is the jet diameter.

A grid dependence study has been performed to assess the dependence of the simulation on the spatial discretisation. The domain is initially discretized by $160 \times 90$ cells, resulting in a constant complete hexahedral grid with $1mm$ cell edge size.

Four grids are created, using telescopic box refinement in a region around the jet. First, a mesh with 2 levels of refinement *(2lvl)* is used, resulting in a canonical mesh with cells of $0.25mm$ edge size near the jet, corresponding to 100 cells on the jet diameter and 36 on the projectile diameter. This mesh has a

resolution equivalent to the mesh used in the three-dimensioned set-up. Then, three finer grids are developed, one with 3 levels of refinement *(3lvl)*, yielding 200 cells on jet diameter, one with 4 levels of refinement *(4lvl)*, yielding 400 cells on jet diameter and finally one with 5 levels of refinement *(5lvl)*, yielding 800 cells on jet diameter and a cell edge of $0.03125mm$.

The jet is placed in the center of the domain. The water-jet and the surrounding air are initially at rest and the pressure is $1bar$. At the beginning of simulation, the bullet starts instantaneously to travel from left to right, at $210^{m}/_{s}$, and hits the jet after approximately $34\mu s$.

## 4. Results

In this section, the numerical results obtained are presented. These are divided into two groups. Initially, 3-D results are presented, followed by high resolution 2-D simulations allowing to capture scales that cannot be resolved in 3-D.

### *4.1. 3-D Simulations*

In figure 2 pressure and vapour structures evolution upon the impact are presented for the 3-D simulation, and then in figure 3 the numerical Schlieren [52] is compared against the experimental shadowgraphy images in different time-steps and is accompanied by the respective velocity and pressure fields. The numerical results are plotted on the vertical and horizontal middle-planes, annotated in figure 1.

When the projectile impacts the water-jet, a shock-wave is released that starts to travel inside the water volume and to expand radially away from the impact point. When the shock reaches and interacts with the deforming interface, it gets reflected as a rarefaction (2a), which is in accordance with the observations of numerous studies [8, 9, 10, 13]. This rarefaction interacts with the shock front, weakens it near the interface and finally splits the high-pressure envelope in two parts (2b), one attached on the solid front and another that propagates towards the opposite free-surface. This shock reflection pattern appears to be similar to the *anomalous reflection* [8, 9, 10].

While the initial shock travels along the convex interface, the incidence angle between the shock front and the interface changes continuously and after a specific point, the reflected rarefactions become more intense and pressure values fall under the saturation threshold and vapour is formed on the periphery of the jet (2b). As the expansion waves cover the region next to the opposite to the entry point free-surface, the cavity expands mainly vertically (2c) and then collapses, emitting pressure waves that travel in the water volume and get reflected on the front free-surface of the jet, again as expansion waves that produce new small vapour cavities (2d).

In fig. 3n it can be seen that the two initially symmetrical vapour cavities, visible in figure 2b, expand mainly on the periphery of the water-jet, following the rarefaction waves, and concentrate in the *catacaustic* region [13] into one

main cavity. The main cavity expands vertically and shrinks horizontally (3o) and finally breaks up into two cavities (3p), which then collapse and vanish.

These results are in qualitative agreement with the experimental data of [1], where the reflection of the initial impact shock-wave on the free-surface of the jet, creates multiple vapour cavities that act as reflective surfaces for upcoming waves. Comparison between the side view experimental shadowgraphy images and the magnitude of the density's gradient from the simulation, plotted on the vertical and horizontal middle plane (fig. 3), indicates that the shock and the cavitation regions (dark regions in experiments and blue iso-surface on simulations) are predicted correctly, as well as the bulk dynamics of the deformation of the free-surface.

In the work of [13] on cavitation induction by confined shocks in spherical droplets, the region of higher cavitation bubble density was identified as the *cat-acaustic* region of shock reflection concentration, near the opposite free-surface. The current numerical results agree with this observation (3n); however, cavitation appears near the opposite free-surface as a later stage of the vapour growth, which is initiated symmetrically on the periphery of the jet (2b). In addition, the vapour cavities do not form or collapse in great proximity to the solid surface, as reported in the experimental data of [1] or suggested for impacts of velocities higher than $100^m/_s$ in [13].

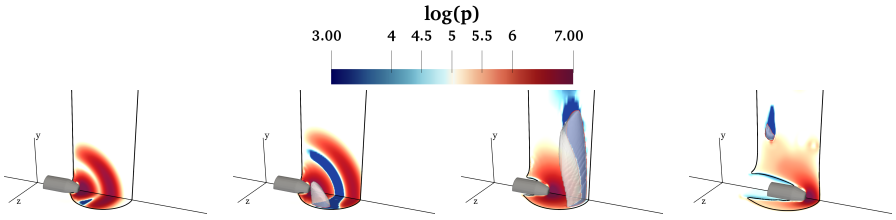


**(a)** $\bar{\tau} = 0.77$ **(b)** $\bar{\tau} = 1.01$ **(c)** $\bar{\tau} = 2.43$ **(d)** $\bar{\tau} = 5.81$

**Figure 2:** Pressure contours in logarithmic scale, *(common logarithm $log_{10}(\cdot)$)*, and vapour volume fraction iso-surface of 0.1% in different time steps are presented for projectile impact on water-jet, at $U_{prj} = 210^m/_s$. 50% iso-line for liquid volume fraction is plotted with black on the vertical and horizontal middle-plane, along with the 0.1% vapour volume fraction with red.

The main characteristics of liquid-to-solid impacts, have been identified by numerous studies [31, 1, 16, 35, 12], and include high-speed jetting, strong shock-waves, with pressures exceeding *water-hammer* value, generation and reflection upon interaction with free-surfaces, rarefactions and potential cavitation induction. Most of these studies regard either spherical or planar droplet impact on solid wall.

The experiment of [1] with the projectile impact on the water-jet tries to expand the knowledge basis of liquid-to-solid impacts on cases of higher velocities. However, the qualitative differences are apparent, as in this case, a projectile of

$9mm$ diameter is impacting a water-jet of $25mm$ diameter and can be fully immersed in to the water volume. Because the solid can be completely immersed in to the water the shock-wave would propagate radially from the solid front, while in the case of a droplet hitting an *infinite wall*, a broader wave front would be generated. Moreover, the contact-edge dynamics would be different as the liquid would have less room to expand in the later case.

### *4.2. 2-D results and discussion*

Although the numerical results presented in the previous section are in agreement with the experimental findings and provide a qualitative insight, the mesh used was not dense enough to capture the detailed jetting phenomena and to provide sharp description of the shocks. Two-dimensional computations were carried out and are presented in this section; this gives the opportunity to achieve high spatial resolution that is computationally impossible to reach with three-dimensional simulations. Moreover, the projectile impact simulation is compared to a case where an infinite flat wall impacts on the water-jet, in order to assess the influence of the corresponding flow blockage which in turn affects the shock-wave emission.

Figure 4 presents the velocity, pressure and density gradient contours, for the four different 2-D grids, at $\bar{\tau} = 1.60$, along with the 50% iso-lines of gas mass and volume fraction, indicating the interface between the water-jet and the ambient air, and the 0.1% isoline of vapour volume fraction, indicating the cavitation region. These results can be compared against results on the vertical mid-plane of the 3-D simulation, as seen in figure 2 and 3i-3p.

The results obtained for the 2-D cases show similar pressure and vapour structures to the three-dimensional configuration. Following the impact, a high-pressure envelope is detached from the contact region and moves towards the opposite free surface. Two low-pressure regions form near the interface of the jet, due to shock reflection as rarefaction, vapour cavities are induced that expand mainly along the periphery of the jet following the reflections and concentrate in the *catacaustic* region [13].

However, in these cases, due to the higher grid density, high-speed jets are easily captured along the solid surface at the entry point. The water, following the violent compression upon the impact, jets out parallel to the solid surface with velocities even 16 times greater than the impact velocity (for the finest grid used), reaching Mach 2.2 with regards to the sonic velocity of the liquid. This is closer to what is observed in experiments on similar impacts [16] and although jetting has been reported in the experiment [1], it was not captured by the three-dimensional simulation.

Comparison of the velocity, pressure and density gradient contours for the four different grids, in figure 4, shows clearly that higher spatial resolution enhances jetting capturing, as well as sharpens the shocks. Moreover, from figure 5, where the instantaneous maximum values of pressure and velocity magnitude, as well as the vapour volume evolution are plotted, it is evident that pressure values converge with mesh refinement, in contrast with velocity

and vapour volume. The higher spacial resolution, finer details of the flow are captured and that is depicted on the diagrams of velocity and vapour.

Refining the computational grid enables to capture finer details of the flow that have strong transient nature, such as the high-speed jetting initiation upon the impact. The coarser grid do not capture the jetting at all, as seen in frame 4a, whereas with additional refinement the jetting becomes first visible (4b), and then less diffused and stronger, as seen in frames 4c and 4d. Moreover, figure 5b, where the maximum velocity magnitude time evolution is plotted for the four grids, shows that for the two finer grids *(4lvl, 5lvl)* supersonic velocities with respect to the liquid are captured, which correspond to the high-speed jets.

In addition, in the results of the finest mesh *(5lvl)*, some perturbations are observed on the liquid-gas interface, that may be related to Richtmyer-Meshkov instability [53]. Richtmyer-Meshkov instability (RMI) arises when a shock-wave accelerates impulsively a density interface. It manifests itself with the formation of wave structures that grow over time, forming mushroom-like protrusions at the interface [53, 54]. It mainly concerns a shock-wave impacting on the interface between gases with different densities [54, 55, 56], but is also observed on liquid-gas interfaces in numerical works [56, 57, 58] and experiments [59]. The RMI finds various applications in combustion systems and mixing [53], scramjet engines [60], Magnetized Target Fusion [58], as well as dissemination of chemical agents [55]. The main mechanism of this instability is the misalignment of the density and pressure gradient, as the shock reflects on the interface, that produces baroclinic torque.

In figure 6, the gradient of the density, along with the vorticity, the baroclinic torque and an estimation of the viscous stresses are presented. This baroclinic torque causes high velocity jetting (fig. 4d), first near the entry point (fig. 6a), that then spreads on the entire periphery of the liquid (fig. 6e) and results in a wavy interface. The dominance of the baroclinic torque in the generation of vorticity and creation of RMI, over the viscous stresses, becomes more clear in frames 6c,6d,6g,6h, where it can be seen that these two sources of vorticity differ by two orders of magnitude. This fact justifies the option to neglect viscosity in the current simulations as well.

Interface roughness plays a role in RMI initiation, where small perturbations of the interface will cause pressure-density gradient misalignment as the shock passes over and will get amplified leading to mashroom shaped spikes. However, as it has been demonstrated by Saurel et al. [59], RMI can be initiated by a shock passing over a simple curved sharp interface, without perturbations. Similar conclusion can be extracted by the current study, where surface roughness on the water-jet interface, present in the experiment, are not considered and RMI occurs on a sharp circular interface.

Moreover, although mesh density affects the vapour formation intensity, as seen in 5c, similar structure is captured by all grids, with the vapour cavity to be initiated on the periphery and finally concentrate on the *catacaustic* region [13]. In contrast, although pressure maxima seem uninfluenced by the mesh refinement, a sharper and more detailed description of the shocks is provided by the denser meshes (*4lvl* in 4c, *5lvl* in 4d), including pressure waves related to

the jets that where absent in the coarsest grid simulation (*2lvl*, 4a).

In order to asses the influence of flow *blockage* on the pressure peaks and high-speed jetting during the solid to jet impact, a two-dimensional planar simulation of a wall impacting a jet is performed and compared to the projectile impact on the jet. This configuration is closer to the geometries reported relevant studies [1, 16, 35, 38].

Comparing the two two-dimensional planar simulations in figure 7, it is apparent that although shock reflection and vapour structures follow similar patterns and jetting is captured in both cases, for the case of the wall, a more homogeneous distribution of higher pressure values is reported, and vapour cavities are initiated further from the solid surface. From the diagram 5a, it can be seen that instantaneous maximum pressure values are higher for the impacting wall rather than the projectile. The high-speed jetting is initially more intense in the case of the projectile, as it can be seen in 7d, 7e, 7f, but the instantaneous maximum velocity reaches higher values for the case of the wall as seen in graph 5b. Finally the vapour production is lower for the impacting wall (5c). These observations confirm that higher *blockage*, or wider solid surface, compresses more the liquid and yields higher pressure values and lower *blockage* intensifies the liquid expansion.

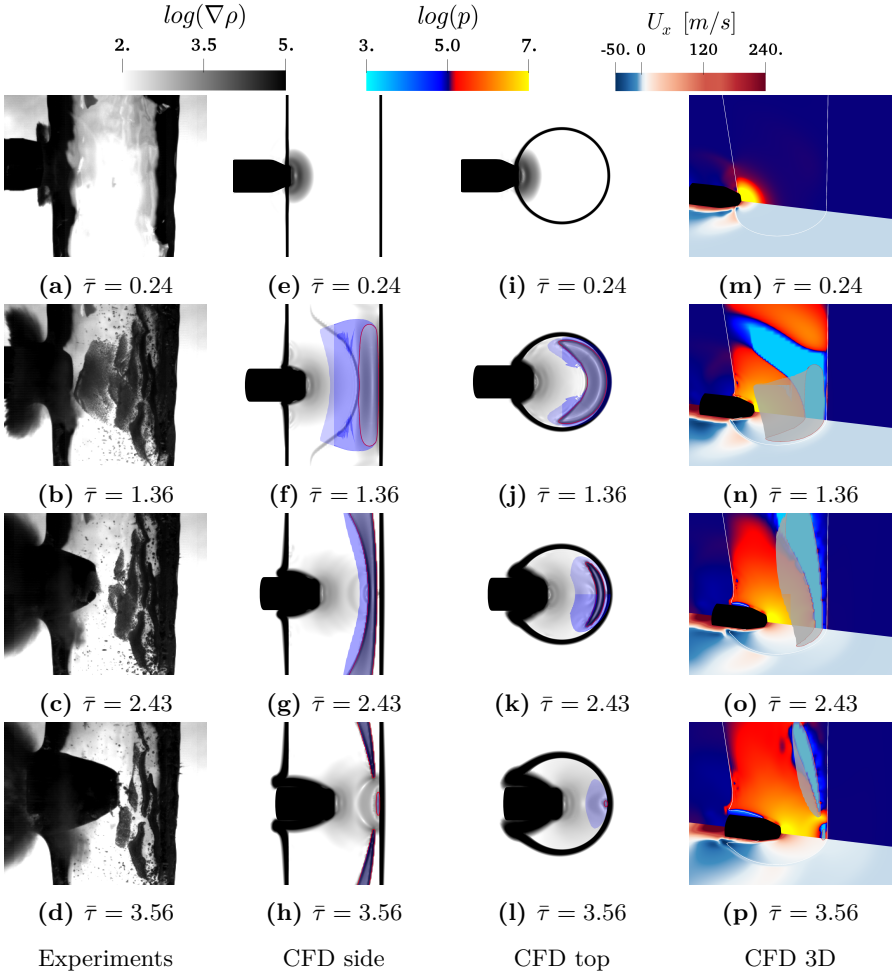


**Figure 3:** Experimental data (a-d) and numerical results (e-p) for the impact of projectile on water-jet, with $U_{prj} = 210^{m}/_{s}$. For the CFD results, the numerical Schlieren [52], computed as the logarithm of the gradient of density, is plotted on the side (e-h) and top (i-l) middle-plane on grey-scale and pressure (vertical plane) and longitudinal velocity component (horizontal plane) contours on the same middle planes (m-p). The vapour is represented by the 0.1% of volume fraction contours, with the blue iso-surface and red iso-lines on the planes on frames (e-l), and the grey iso-surface on frames (m-p). The common logarithm $log_{10}(\cdot)$ is used in for the density and pressure fields.

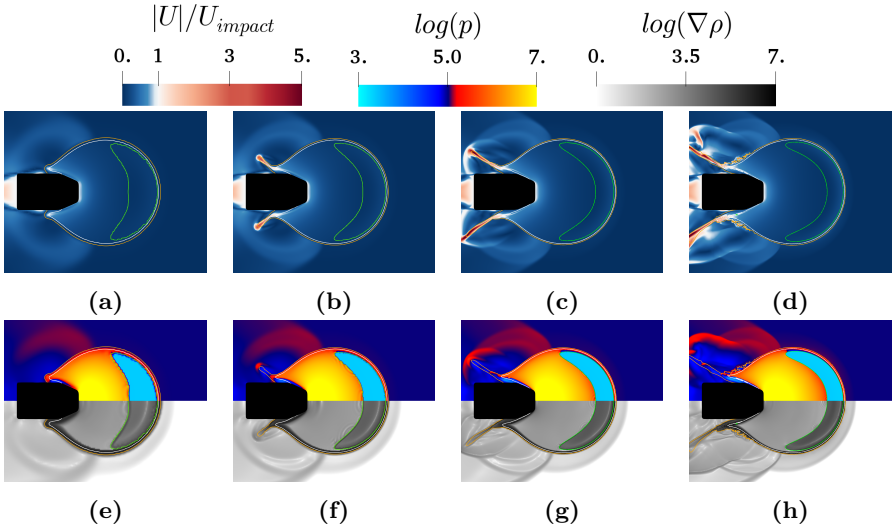


**Figure 4:** Comparison of velocity magnitude (a-d), normalized with the impact velocity $U_{impact} = 210^{m}/_{s}$, at $\bar{\tau} = 1.60$, pressure (upper half) and the numerical Schlieren [52] (lower half) contours in logarithmic scale (e-h) *(common logarithm $log_{10}(\cdot)$)*, for solid projectile impact on two-dimensional planar water-jet, for the four different meshes: (a,e) *2lvl - 100 cells/$D_{jet}$*, (b,f) *3lvl - 200 cells/$D_{jet}$*, (c,g) *4lvl - 400 cells/$D_{jet}$*, (d,h) *5lvl - 800 cells/$D_{jet}$*. The isolines of 50% gas mass fraction is plotted with orange color and 50% gas volume fraction contour with white to represent the interface between ambient air and water-jet. The 0.1% isoline of vapour volume fraction is visible with green.

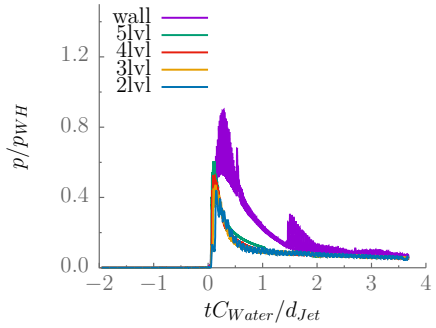


**(a)**

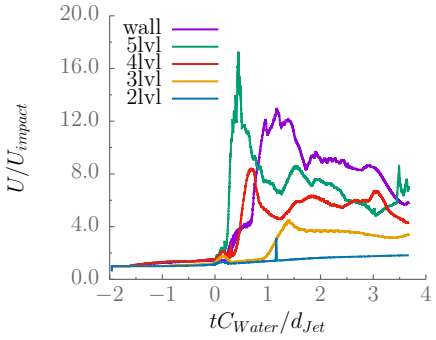


**(b)**

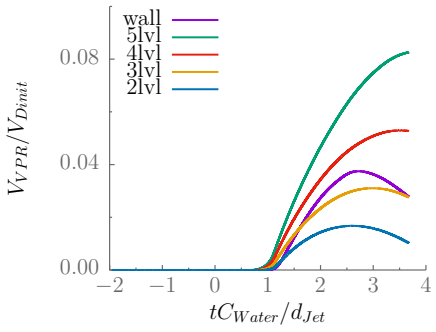


**(c)**

**Figure 5:** Comparison of different 2D meshes for projectile impact on jet: (a) Maximum pressure normalized with water hammer pressure ($P_{WH} = 398.7MPa$) (b) Maximum Velocity magnitude normalized with impact velocity $U_{imp} = 210^{m}/_{s}$, (c) Vapour Volume ($V_{VPR}$) normalized with the initial volume of the water-jet ($V_{Dinit}$). The equivalent results from the wall impact on the jet (using the *4lvl* mesh) are also plotted (purple line) for demonstration of the influence of the *blockage*.

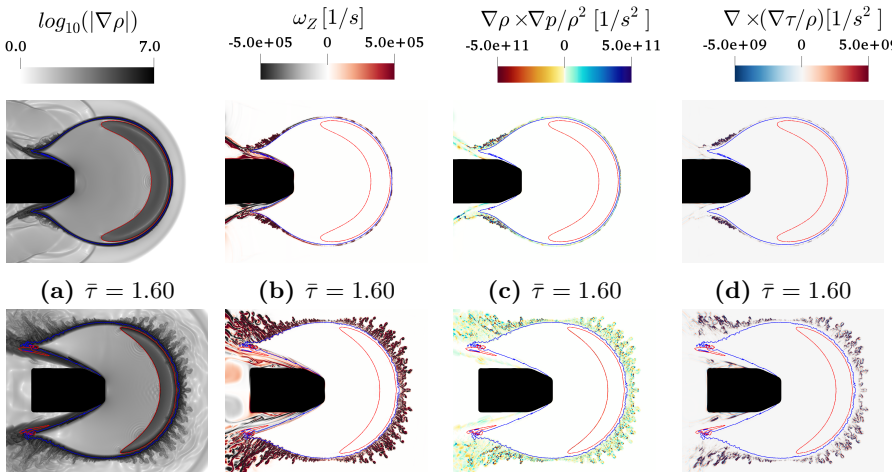


**(a)** $\bar{\tau} = 1.60$ **(b)** $\bar{\tau} = 1.60$ **(c)** $\bar{\tau} = 1.60$ **(d)** $\bar{\tau} = 1.60$

**(e)** $\bar{\tau} = 3.38$ **(f)** $\bar{\tau} = 3.38$ **(g)** $\bar{\tau} = 3.38$ **(h)** $\bar{\tau} = 3.38$

**Figure 6:** Evidence of Richtmyer-Meshkov instability [53] for solid projectile impact on two-dimensional planar water-jet. From left to right: numerical Schlieren [52] contours in logarithmic scale *(common logarithm $log_{10}(\cdot)$)*, vorticity contours ($\omega_z$ $[1/s]$), baroclinic torque ($\nabla\rho \times \nabla p/\rho^2[1/s^2]$), viscous shear stresses ($\nabla \times (\nabla\tau/\rho)[1/s^2]$). For the estimation of viscous stresses, which are neglected in the simulation, dynamic viscosity is given by $\mu = (1 - \alpha_{gas}) \cdot \mu_{liquid} + \alpha_{gas} \cdot \mu_{gas}$, based on gas volume fraction, with $\mu_{liquid} = (1 - \alpha_{vapour}) \cdot \mu_{water} + \alpha_{vapour} \cdot \mu_{vapour}$ and $\mu_{water} = 9.99 \times 10^{-4} Ns/m^2$, $\mu_{vapour} = 9.99 \times 10^{-6} Ns/m^2$, $\mu_{gas} = 1.84 \times 10^{-5} Ns/m^2$. Results of the simulation using the *5lvl* mesh *(800 cells/$D_{jet}$)*. The isolines of 50% gas volume fraction contour, which represents the interface between ambient air and water-jet, is plotted with blue and of 0.1% vapour volume fraction with red.

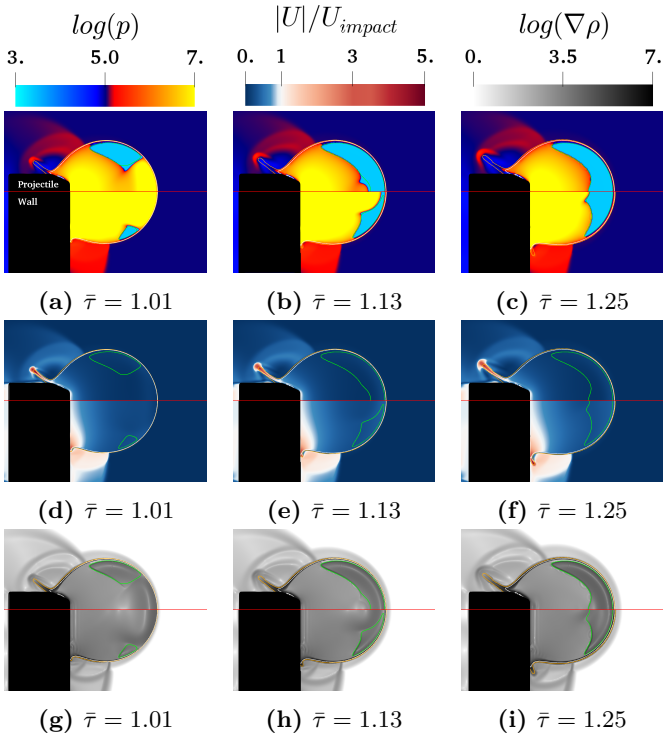


**(a)** $\bar{\tau} = 1.01$ **(b)** $\bar{\tau} = 1.13$ **(c)** $\bar{\tau} = 1.25$

**(d)** $\bar{\tau} = 1.01$ **(e)** $\bar{\tau} = 1.13$ **(f)** $\bar{\tau} = 1.25$

**(g)** $\bar{\tau} = 1.01$ **(h)** $\bar{\tau} = 1.13$ **(i)** $\bar{\tau} = 1.25$

**Figure 7:** Contours of pressure in logarithmic scale (a-c), velocity magnitude normalized with the impact velocity $U_{impact} = 210m/s$ (d-f) and the numerical Schlieren [52] in logarithmic scale (g-i) for solid projectile (upper half) and solid wall (lower half) impact on two-dimensional planar water-jet. The IB body (black region of left) moves from left to right. 50% gas mass fraction is plotted with orange color and 50% gas volume fraction contour with white to represent the interface between ambient air and water-jet. The 0.1% isoline of vapour volume fraction is visible with green. The *4lvl* mesh is used in both cases. The common logarithm $log_{10}(\cdot)$ is used in for the density and pressure fields.

| Mesh | Cells | $dx_{min}$ [mm] | $dt_{mean}$ [s] | CPUh | $T_{mean}$ per iter [s] |
|---|---|---|---|---|---|
| 3D | 2.9M | 0.192 | 5.27e-9 | 4358 | 24.92 |
| 2D-2lvl | 40k | 0.250 | 7.45e-9 | 18 | 1.250 |
| 2D-3lvl | 120k | 0.125 | 3.51e-9 | 432 | 4.790 |
| 2D-4lvl | 375k | 0.063 | 1.33e-9 | 2621 | 13.23 |
| 2D-5lvl | 1.2M | 0.031 | 0.91e-9 | 31261 | 20.82 |

**Table 1:** Computational cost (in *CPU-hours*) for the 3D and 2D simulations, along with indicative clock time for completion of one iteration/time-step *($T_{mean}$ per iter.)* and characteristic spatial and temporal resolution *($dx_{min}$ and $dt_{mean}$).*

### *4.3. Computational Cost*

The importance of the high-resolution two-dimensional simulations is apparent from the level of detail unveiled in comparison with the three-dimensional case. The cost for a 3-D computation of an equivalent resolution is prohibiting. As it can be seen in table 1, the computational cost increases rapidly as the grid gets finer and for the *2D-5lvl* mesh is 7 times higher that for the *3D* mesh. The presence of the IB source term in the equations 2.2, which receives high values, dictates strict time-step restrictions and thus for all the simulations the Courant number is limited below 0.05.

The simulations where carried out mainly on a workstation equipped with a Intel Xeon E5-2690 V3 @2.6$GHz$, with 2 sockets of 12 double thread cores each, with hyper-threading enabled. Depending on the total cell count from 4 up to 40 cores have been used. A cluster computer was also used to accelerate the simulation of the finest 2-D mesh *(5lvl)*, where 96 CPUs have been used.

## 5. Conclusions

The current paper examined the solid projectile impact on a water-jet and assessed the use of direct-forcing Immersed Boundary Method in conjunction with an explicit density-based compressible two-phase solver that accounts for cavitation. This problem has been studied so far only qualitatively as reported by the experimental data of[1]; the current study is the first to simulate this experiment and makes an attempt to quantify the experiment's findings.

To make this possible, a newly developed numerical framework has been applied, involving moving solid boundaries and an alternative to the more complex cut-cell Immersed Boundary methodologies for cavitating flows [42, 43, 44]. A direct-forcing approach is used, where the immersed solid is modelled through adding body force source terms in the compressible momentum equations. The solver accounts for gaseous and liquid phases and supports phase-change following a barotropic law. The presented numerical tool was proven capable of handling complicated highly compressible cavitating flows.

The underlying physical processes of the simulated case was found to be in qualitative agreement with the relevant experimental observations of [1]. Pressure shock-waves, rarefaction waves and cavitation formation, development and subsequent collapse, that follow the impact are numerically captured. A detailed description of the vapour cavity was provided that was in accordance with the analysis of the experimental data. High-speed jetting was also observed in the simulations, although was found highly dependent on the grid resolution of the jet interface, near the impact region, and therefore was captured on the two-dimensional simulations, where the use of denser meshes was less CPU time demanding.

Finally, the influence of flow blockage on the dynamics of the impact was assessed by comparing the case of the projectile to the case of a wall hitting the water target. The study showed that in the case of the projectile, where the liquid is free to expand in the direction of the projectile motion, the pressure and velocity peaks during the initial stage of the impact reach lower values than in the case of the wall; in this case, the flow was found to decelerate faster, whereas the vapour production was higher for the projectile case.

## Acknowledgement

This work was carried out in the framework of CaFE project, which has received funding from the European Union Horizon 2020 Research and Innovation programme, with Grant Agreement No 642536.

## References

[1] J. Field, J.-J. Camus, M. Tinguely, D. Obreschkow, M. Farhat, Cavitation in impacted drops and jets and the effect on erosion damage thresholds, Wear 290–291 (2012) 154–160. doi:10.1016/j.wear.2012.03.006.

URL http://www.sciencedirect.com/science/article/pii/S0043164812000968

[2] P. A. Engel, Chapter 11—Liquid Erosion, in: P. A. Engel (Ed.), Impact Wear of Material, Vol. 2 of Tribology Series, Elsevier, 1978, pp. 291–319. doi:10.1016/S0167-8922(09)70036-7.
URL http://www.sciencedirect.com/science/article/pii/S0167892209700367

[3] F. Heymann, Erosion by liquids, Machine Design 10 (1970) 118–124.

[4] S. Abrate, Soft impacts on aerospace structures, Progress in Aerospace Sciences 81 (Supplement C) (2016) 1–17, dynamic Loading Aspects of Composite Materials. doi:10.1016/j.paerosci.2015.11.005.
URL http://www.sciencedirect.com/science/article/pii/S0376042115300294

[5] P. O. K. Krehl, History of Shock Waves, Explosions and Impact, Springer-Verlag GmbH, 2009. doi:10.1007/978-3-540-30421-0.

[6] P. Koukouvinis, M. Gavaises, O. Supponen, M. Farhat, Simulation of bubble expansion and collapse in the vicinity of a free surface, Physics of Fluids 28 (5) (2016) 052103.

[7] T. Leighton, The acoustic bubble, Academic press, 2012.

[8] J. W. Grove, R. Menikoff, Anomalous reflection of a shock wave at a fluid interface, Journal of Fluid Mechanics 219 (1990) 313–336. doi:10.1017/S0022112090002968.

[9] R.R. Nourgaliev and S.Y. Sushchikh and T.N. Dinh and T.G. Theofanous, Shock wave refraction patterns at interfaces, International Journal of Multiphase Flow 31 (9) (2005) 969–995. doi:10.1016/j.ijmultiphaseflow.2005.04.001.
URL http://www.sciencedirect.com/science/article/pii/S0301932205000753

[10] H. Hosseini, S. Moosavi-Nejad, H. Akiyama, V. Menezes, Shock wave interaction with interfaces between materials having different acoustic impedances, Applied Physics Letters 104 (10) (2014) 103701.
URL https://doi.org/10.1063/1.4867883

[11] N. A. Hawker, Y. Ventikos, Interaction of a strong shockwave with a gas bubble in a liquid medium: a numerical study, Journal of Fluid Mechanics 701 (2012) 59–97. doi:10.1017/jfm.2012.132.

[12] K. K. Haller, D. Poulikakos, Y. Ventikos, P. Monkewitz, Shock wave formation in droplet impact on a rigid surface: lateral liquid motion and multiple wave structure in the contact line region, Journal of Fluid Mechanics 490 (2003) 1–14. doi:10.1017/S0022112003005093.

[13] D. Obreschkow, N. Dorsaz, P. Kobel, A. de Bosset, M. Tinguely, J. Field, M. Farhat, Confined shocks inside isolated liquid volumes: A new path of erosion?, Physics of Fluids 23 (10) (2011) 101702.
URL https://doi.org/10.1063/1.3647583

[14] T. Obara, N. Bourne, J. Field, Liquid-jet impact on liquid and solid surfaces, Wear 186-187 (Part 2) (1995) 388–394, 8th International Conference on Erosion by Liquid and Solid Impact. doi:10.1016/0043-1648(95)07187-3.
URL http://www.sciencedirect.com/science/article/pii/0043164895071873

[15] N. K. Bourne, T. Obara, J. E. Field, The Impact and Penetration of a Water Surface by a Liquid Jet, Proceedings: Mathematical, Physical and Engineering Sciences 452 (1949) (1996) 1497–1502.
URL http://www.jstor.org/stable/52928

[16] J. E. Field, M. B. Lesser, J. P. Dear, Studies of Two-Dimensional Liquid-Wedge Impact and Their Relevance to Liquid-Drop Impact Problems, Proceedings of the Royal Society of London. Series A, Mathematical and Physical Sciences 401 (1821) (1985) 225–249.
URL http://0-www.jstor.org.wam.city.ac.uk/stable/2397887

[17] J. Field, J. Dear, J. Ogren, The effects of target compliance on liquid drop impact, Journal of Applied Physics 65 (2) (1989) 533–540.
URL http://aip.scitation.org/doi/pdf/10.1063/1.343136

[18] F. P. Bowden, J. H. Brunton, The Deformation of Solids by Liquid Impact at Supersonic Speeds, Proceedings of the Royal Society of London. Series A, Mathematical and Physical Sciences 263 (1315) (1961) 433–450.
URL http://0-www.jstor.org.wam.city.ac.uk/stable/2414324

[19] J. Brunton, A discussion on deformation of solids by the impact of liquids, and its relation to rain damage in aircraft and missiles, to blade erosion in steam turbines, and to cavitation erosion - High speed liquid impact, Philosophical Transactions of the Royal Society of London A: Mathematical, Physical and Engineering Sciences 260 (1110) (1966) 79–85. arXiv:http://rsta.royalsocietypublishing.org/content/260/1110/79.full.pdf, doi:10.1098/rsta.1966.0031.
URL http://rsta.royalsocietypublishing.org/content/260/1110/79

[20] H. W. Bargmann, The mechanics of erosion by liquid and solid impact, International Journal of Solids and Structures 29 (14) (1992) 1685–1698. doi:10.1016/0020-7683(92)90162-M.
URL http://www.sciencedirect.com/science/article/pii/002076839290162M

[21] F. P. Bowden, J. E. Field, The Brittle Fracture of Solids by Liquid Impact, by Solid Impact, and by Shock, Proceedings of the Royal Society of London. Series A, Mathematical and Physical Sciences 282 (1390) (1964) 331–352.
URL http://0-www.jstor.org.wam.city.ac.uk/stable/2414778

[22] M. Hoogenboom, D. Eikelenboom, M. H. den Brok, A. Heerschap, J. J. Fütterer, G. J. Adema, Mechanical high-intensity focused ultrasound destruction of soft tissue: working mechanisms and physiologic effects, Ultrasound in Medicine and Biology 41 (6) (2015) 1500–1517.
URL https://doi.org/10.1016/j.ultrasmedbio.2015.02.006

[23] W. Mingxi, Y. Feng, G. T. Haar, Cavitation in Biomedicine: Principles and Techniques, Springer, 2015.

[24] C. Leiber, Assessment of safety and risk with a microscopic model of detonation, Elsevier, 2003.

[25] Y.-T. Wu, A. Adnan, Effect of Shock-Induced Cavitation Bubble Collapse on the damage in the Simulated Perineuronal Net of the Brain, Scientific reports 7 (1) (2017) 5323. doi:10.1038/s41598-017-05790-3.

[26] G. S. Nusholtz, E. B. Wylie, L. G. Glascoe, Internal cavitation in simple head impact model, Journal of neurotrauma 12 (4) (1995) 707–714.
URL https://doi.org/10.1089/neu.1995.12.707

[27] G. S. Nusholtz, L. G. Glascoe, E. B. Wylie, Cavitation during head impact, Tech. rep., SAE Technical Paper (1997).
URL https://doi.org/10.4271/970390

[28] P. Koukouvinis, C. Bruecker, M. Gavaises, Unveiling the physical mechanism behind pistol shrimp cavitation, Scientific Reports 7 (1) (2017) 13994. doi:10.1038/s41598-017-14312-0.

[29] S. Patek, W. Korff, R. Caldwell, Biomechanics: deadly strike mechanism of a mantis shrimp, Nature 428 (6985) (2004) 819.

[30] L. Davison, Fundamentals of shock wave propagation in solids, Springer Science & Business Media, 2008.

[31] M. B. Lesser, Analytic Solutions of Liquid-Drop Impact Problems, Proceedings of the Royal Society of London. Series A, Mathematical and Physical Sciences 377 (1770) (1981) 289–308.
URL http://0-www.jstor.org.wam.city.ac.uk/stable/2397187

[32] S. T. Thoroddsen, T. G. Etoh, K. Takehara, Y. Takano, Impact jetting by a solid sphere, Journal of Fluid Mechanics 499 (2004) 139–148. doi:10.1017/S0022112003007274.

[33] F. H. Harlow, J. P. Shannon, The Splash of a Liquid Drop, Journal of Applied Physics 38 (10) (1967) 3855–3866. arXiv:https://doi.org/10.1063/1.1709031, doi:10.1063/1.1709031.
URL https://doi.org/10.1063/1.1709031

[34] D. J. Harvie, D. F. Fletcher, A hydrodynamic and thermodynamic simulation of droplet impacts on hot surfaces, Part I: theoretical model, International Journal of Heat and Mass Transfer 44 (14) (2001) 2633–2642. doi:10.1016/S0017-9310(00)00303-3.
URL http://www.sciencedirect.com/science/article/pii/S0017931000003033

[35] T. Sanada, K. Ando, T. Colonius, A computational study of high-speed droplet impact, Fluid Dynamics & Materials Processing 7 (4) (2011) 329–340.

[36] Y.-Y. Niu, H.-W. Wang, Simulations of the shock waves and cavitation bubbles during a three-dimensional high-speed droplet impingement based on a two-fluid model, Computers & Fluids 134-135 (2016) 196–214. doi:10.1016/j.compfluid.2016.05.018.
URL http://www.sciencedirect.com/science/article/pii/S0045793016301657

[37] Nikolaos Kyriazis and Phoevos Koukouvinis and Manolis Gavaises, Modelling cavitation during drop impact on solid surfaces, Advances in Colloid and Interface Sciencedoi:10.1016/j.cis.2018.08.004.
URL http://www.sciencedirect.com/science/article/pii/S0001868618301398

[38] Q. Zhou, N. Li, X. Chen, T. Xu, S. Hui, D. Zhang, Liquid drop impact on solid surface with application to water drop erosion on turbine blades, Part II: Axisymmetric solution and erosion analysis, International Journal of Mechanical Sciences 50 (10) (2008) 1543–1558. doi:10.1016/j.ijmecsci.2008.08.002.
URL http://www.sciencedirect.com/science/article/pii/S0020740308001197

[39] C. S. Peskin, Numerical analysis of blood flow in the heart, Journal of Computational Physics 25 (3) (1977) 220–252. doi:10.1016/0021-9991(77)90100-0.
URL http://www.sciencedirect.com/science/article/pii/0021999177901000

[40] R. Mittal, G. Iaccarino, Immersed Boundary Methods, Annual Review of Fluid Mechanics 37 (1) (2005) 239–261. arXiv:http://dx.doi.org/10.1146/annurev.fluid.37.061903.175743, doi:10.1146/annurev.fluid.37.061903.175743.
URL http://dx.doi.org/10.1146/annurev.fluid.37.061903.175743

[41] L. Mochel, P.-É. Weiss, S. Deck, Zonal Immersed Boundary Conditions: Application to a High-Reynolds-Number Afterbody Flow, AIAA Journal 52 (12) (2014) 2782–2794. doi:10.2514/1.J052970.
URL http://dx.doi.org/10.2514/1.J052970

[42] F. Örley, V. Pasquariello, S. Hickel, N. A. Adams, Cut-element based immersed boundary method for moving geometries in compressible liquid flows with cavitation., J. Comput. Physics 283 (2015) 1–22.
URL http://dblp.uni-trier.de/db/journals/jcphy/jcphy283.html#OrleyPHA15;http://dx.doi.org/10.1016/j.jcp.2014.11.028;http://www.bibsonomy.org/bibtex/254f14dc8931bde4b39d5485d757c826b/dblp

[43] C. Huang, J. Huang, Y. Wang, C. Xu, Cloud cavitating flow around an axisymmetric projectile in the shallow water, in: 10th International Cavitation Symposium, 2018.

[44] S. Lee, S. Park, S. H. Rhee, J. Seo, 6DOF motion and Cavity Dynamics of a Ventilated Super-cavitating Vehicle with Control Fins, in: 10th International Cavitation Symposium, 2018.

[45] H. G. Weller, G. Tabor, H. Jasak, C. Fureby, A tensorial approach to computational continuum mechanics using object-oriented techniques, Computers in Physics 12 (6) (1998) 620–631. arXiv:https://aip.scitation.org/doi/pdf/10.1063/1.168744, doi:10.1063/1.168744.
URL https://aip.scitation.org/doi/abs/10.1063/1.168744

[46] J.-P. Franc, J.-M. 1932 Michel, Fundamentals of cavitation, Vol. 76., Kluwer Academic Publishers, Dordrecht;London;, 2004.

[47] E. Brennen C., Cavitation and Bubble Dynamics, 1995.

[48] J. H. Seo, R. Mittal, A sharp-interface immersed boundary method with improved mass conservation and reduced spurious pressure oscillations, Journal of Computational Physics 230 (19) (2011) 7347–7363. doi:10.1016/j.jcp.2011.06.003.
URL http://www.sciencedirect.com/science/article/pii/S0021999111003524

[49] F. Örley, T. Trummler, S. Hickel, M. S. Mihatsch, S. J. Schmidt, N. A. Adams, Large-eddy simulation of cavitating nozzle flow and primary jet break-up, Physics of Fluids 27 (8) (2015) 086101. arXiv:http://aip.scitation.org/doi/pdf/10.1063/1.4928701, doi:10.1063/1.4928701.
URL http://aip.scitation.org/doi/abs/10.1063/1.4928701

[50] N. Adams, D. Rahn, S. Schmidt, T. Trummler, Large Eddy simulation of cavitating nozzle flows and primary jet break-up with gas-entrainment into the nozzle, in: 10th International Cavitation Symposium, 2018.

[51] S. Schmidt, I. Sezal, G. Schnerr, M. Talhamer, Riemann techniques for the simulation of compressible liquid flows with phase-transistion at all Mach numbers-shock and wave dynamics in cavitating 3-D micro and macro systems, in: 46th AIAA aerospace sciences meeting and exhibit, 2008, p. 1238.

[52] G. S. Settles, M. J. Hargather, A review of recent developments in schlieren and shadowgraph techniques, Measurement Science and Technology 28 (4) (2017) 042001.
URL http://stacks.iop.org/0957-0233/28/i=4/a=042001

[53] M. Brouillette, The Richtmyer-Meshkov instability, Annual Review of Fluid Mechanics 34 (1) (2002) 445–468.

[54] R. L. Holmes, G. Dimonte, B. Fryxell, M. L. Gittings, J. W. Grove, M. Schneider, D. H. Sharp, A. L. Velikovich, R. P. Weaver, Q. Zhang, Richtmyer–Meshkov instability growth: experiment, simulation and theory, Journal of Fluid Mechanics 389 (1999) 55–79.

[55] C.-H. Chang, X. Deng, T. G. Theofanous, Direct numerical simulation of interfacial instabilities: a consistent, conservative, all-speed, sharp-interface method, Journal of Computational Physics 242 (2013) 946–990.
URL https://doi.org/10.1016/j.jcp.2013.01.014

[56] S. Lugomer, Laser generated Richtmyer–Meshkov instability and nonlinear wave paradigm in turbulent mixing: I. Central region of Gaussian spot, Laser and Particle Beams 34 (4) (2016) 687–704. doi:10.1017/S0263034616000598.

[57] V. Suponitsky, A. Froese, S. Barsky, Richtmyer–Meshkov instability of a liquid–gas interface driven by a cylindrical imploding pressure wave, Computers & Fluids 89 (2014) 1–19.
URL https://doi.org/10.1016/j.compfluid.2013.10.031

[58] R. Samulyak, Y. Prykarpatskyy, Richtmyer–Meshkov instability in liquid metal flows: influence of cavitation and magnetic fields, Mathematics and Computers in Simulation 65 (4) (2004) 431–446, wave Phenomena in Physics and Engineering: New Models, Algorithms, and Applications. doi:10.1016/j.matcom.2004.01.019.
URL http://www.sciencedirect.com/science/article/pii/S0378475404000278

[59] R. Saurel, F. Petitpas, R. A. Berry, Simple and efficient relaxation methods for interfaces separating compressible fluids, cavitating flows and shocks in multiphase mixtures, Journal of Computational Physics 228 (5) (2009) 1678–1712. doi:10.1016/j.jcp.2008.11.002.
URL http://www.sciencedirect.com/science/article/pii/S0021999108005895

[60] Q. Yang, J. Chang, W. Bao, Richtmyer-Meshkov Instability Induced Mixing Enhancement in the Scramjet Combustor with a Central Strut, Advances in Mechanical Engineering 6 (2014) 614189. arXiv:https://doi.org/10.1155/2014/614189, doi:10.1155/2014/614189.
URL https://doi.org/10.1155/2014/614189